On the spherically symmetrical combustion of methyl decanoate droplets and comparisons with detailed numerical modeling

Yu Cheng Liu [a],*, Tanvir Farouk [b],*, Anthony J. Savas [a], Frederick L. Dryer [c], C. Thomas Avedisian [a]

[a] *Sibley School of Mechanical and Aerospace Engineering, Cornell University, Ithaca, NY 14853, USA*
[b] *Department of Mechanical Engineering, University of South Carolina, Columbia, SC 29208, USA*
[c] *Department of Mechanical and Aerospace Engineering, Princeton University, Princeton, NJ 08544, USA*

ABSTRACT

This study presents an experimental effort and detailed numerical simulation of the burning process of an ester-based biodiesel fuel droplet – methyl decanoate (MD). The experiments are carried out using test droplets that are anchored to small SiC support structures (14 μm diameter) and that burn in an ambience subjected to a low gravity level to promote spherical symmetry in the droplet burning process. The initial droplet diameters are 0.53–0.57 mm and the combustion gas is normal atmospheric pressure air. A detailed numerical simulation of the burning process is also presented that features detailed MD combustion chemistry, radiative heat transfer, species diffusion, and phase change effects to predict the evolution of droplet and flame diameter. The analysis also incorporates a model for heat transfer through the droplet support structure.

Predicted droplet and flame diameters are shown to agree within the range of uncertainty of the experimental data lending support to the transport model and combustion kinetics incorporated in the simulation. Effects of the tether fiber's size, thermal conductivity, and Nusselt number on the droplet burning data are also examined. Results show that the fiber properties within the range investigated in this study do not significantly affect the burning process. Species and temperature distributions during the transient process of MD droplet combustion are detailed in this study. These comparisons and predictions for multi-phase combustion of MD that have not been seen in the literature provide validation for MD models associated with chemical kinetics and multi-physics and are therefore valuable for the study of ester-based biodiesel combustion.

© 2012 The Combustion Institute. Published by Elsevier Inc. All rights reserved.

1. Introduction

Liquid fuels have dominated transportation systems for over a century and they will continue to do so for decades to come [1,2]. Sustainable energy technologies (e.g., wind, solar, electric) are not at the stage where they will significantly impact liquid transportation fuel use. While such sustainable concepts are being developed, improvements in the efficiency of the internal combustion engine stand to have an immediate impact on reducing transportation fuel consumption and combustion emissions. Of the two main engine types – compression (CI) and spark ignition (SI) – the efficiency of CI engines is higher (i.e., 40–50% for CI compared to 25–30% for SI). As such, diesel power has the potential for an immediate impact on petroleum consumption, especially when conventional diesel is blended with bio-diesel fuels [3–5].

Blending diesel fuel with a fuel derived from sustainable sources will have an immediate impact on petroleum consumption

[6,7]. First generation biodiesels derived from vegetable oils such as soybean and rapeseed oils are typically produced by reaction of the bio-oil with an alcohol (e.g., methanol, ethanol, etc.) to form methyl ester mixtures (the "biodiesel") and glycerol [8,9]. Considering as an example rapeseed oil as the biofeedstock, the rapeseed methyl ester (RME) biodiesel that results from this process is considered to be comprised of five mostly unsaturated C_{17} to C_{19} [10,11] or C_{14} to C_{22} methyl esters [12].

The complexity of biodiesels makes it difficult to develop oxidation schemes and physical property estimates needed to carry out numerical analysis of in-cylinder combustion processes [3,13], and a thorough knowledge of fuel property and combustion chemistry effects is also needed. Moreover, it is difficult to perform fundamental experiments to develop the kinetic models because of the difficulty in producing fully pre-vaporized fuel/oxidizer mixtures and in sampling the intermediates produced during combustion. Surrogates are an attractive, if not necessary, alternative to alleviating these concerns. Surrogates are blends of well-characterized components that represent broad chemical classes of a real fuel, with the fractional amounts of the constituents chosen to replicate

certain combustion "targets" of the real fuel [14,15]. Much work has been reported to develop the combustion chemistry of biodiesel surrogates.

Methyl butanoate (MB, boiling point of 375 K) combustion chemistry was originally developed by Fisher et al. [16] because of MB's potential as a biodiesel surrogate. It was subsequently considered that MB is too simple to simulate biodiesel as it does not represent its autoignition characteristics, particularly at low temperatures [17,18]. Herbinet et al. [11] noted that the larger methyl decanoate molecule (MD, boiling point of 497 K) better represented the kinetics of RME for the jet-stirred reactor (JSR) data of Dagaut et al. [12] than did smaller methyl ester molecules (e.g., MB). Most recently, the MD combustion kinetics was improved to include both high and low temperature oxidation chemistry [17].

The development and evaluation of biodiesel surrogates was previously carried out with combustion targets derived from gaseous/pre-vaporized fuels using experimental designs that promoted zero-dimensional (homogeneous) or one-dimensional gas transport. The experimental configurations include shock tubes (ST), counterflow flames (CFF), and JSR and flow reactors (FR) all of which figured prominently in the development of MD combustion chemistry when coupled with detailed numerical simulation. For example, Gaïl et al. [17] reported computational simulations of JSR, FR and a premixed CFF to guide modifications of a previously developed kinetic mechanism for MB. And Sheshadri et al. [18] used the MD combustion kinetics presented in [11] to predict ignition and extinction conditions of MD for a non-premixed CFF.

No studies have provided a detailed account on the efficacy of the oxidation chemistry of biodiesels to predict targets derived from combustion of a liquid biodiesel. A first step is to select an appropriate configuration to develop combustion targets from a liquid fuel combustion configuration that can be modeled, and for which the targets can be accurately measured. A second step is to apply a detailed numerical simulation of the configuration to predict the targets and compare with measured values. The present study accomplishes both objectives.

Regarding a suitable combustion configuration for liquid fuels, at one extreme is the stochastic in-cylinder environment of a CI engine, which incorporates a swirling and turbulent motion that is extremely difficult to model. Sprays set the initial conditions for engine combustion but simulating a burning spray is currently beyond the scope of detailed numerical simulation owing to multiphase and moving boundary behavior and interaction effects among the constituent droplets. For example, biodiesel combustion in an engine with spray injection was simulated [3,13] using the KIVA-ERC-Chemkin code [19,20] with sub-models to predict soot and NO_x emissions, and which identified the importance of vapor heat capacity and liquid density. A motored Co-operative Fuel Research (CFR) engine was simulated [21,22] with the combustion chemistry taken from [10] to investigate the auto-ignition, heat release, and CO and CO_2 emissions of pre-vaporized MD delivered through a fuel intake design that minimized the presence of droplets in the engine and produced a premixed gas stream. The results explained the comparatively high CO_2 levels at low compression ratios compared to conventional diesel fuels. This same combustion chemistry was later found to represent well extinction and ignition of MD in a laminar non-premixed counterflow configuration with appropriate modifications [18].

At the other extreme is a combustion configuration that incorporates a tractable fundamental geometry and laminar conditions so as to permit detailed simulations of the combustion event. The corresponding canonical geometry for liquid fuels is that of an isolated droplet burning under conditions where there is no relative velocity between the droplet and surrounding gas, and for which the flow is created entirely by the evaporation process. Under these conditions, the streamlines of the flow will be radial and a one-dimensional gas phase symmetric condition will be created. The flame will then be spherical and concentric with the droplet. Figure 1 shows this configuration.

The relevance of the configuration of Fig. 1 has been established by Sirignano [23] (and many others) who noted that the spherically symmetric droplet burning configuration incorporates many fundamental physical processes that remain even as the flow field becomes complex (e.g., as in sprays), including transient heat conduction and mass diffusion, phase equilibrium at the interface and the moving boundary of the liquid surface. Combustion targets in Fig. 1 that can assist these efforts include the evolution of flame, droplet diameter and burning rate [24,25]. If the fuel under consideration produces soot, the proximity of the soot shell to the droplet (not shown in Fig. 1) provides another target. And if the flame extinguishes, the droplet diameter at extinction is an important metric to identify extinction mechanisms [26].

The radial symmetry shown in Fig. 1 facilitates incorporating complex processes in modeling that would otherwise be prohibitive to include, such as variable property effects (both temperature and compositional dependencies), radiative losses from the flame, and complex combustion chemistry, all of which are well beyond the assumptions of the classical theory of droplet combustion [23]. In this way, important characteristics of droplet burning can be modeled that are still relevant beyond the simplified configuration shown in Fig. 1. For example, the ignition delay time of MD droplets has been measured at elevated ambient temperatures [27] to identify mechanisms for the increase of NO_x often found for biodiesels. These mechanisms are intrinsic to the combustion process and are expected to carry over to more complex droplet evaporation configurations. A numerical analysis of spherically symmetric droplet burning for methanol [26] showed the influence of CO_2 as an inert in the ambient gas on the mechanism for extinction as diffusive or radiative, as well as the influence of initial droplet size on the droplet diameter at extinction.

In the present study, we report the results of an experimental and numerical study of MD droplet burning under conditions designed to promote the configuration of Fig. 1. The results presented here show the extent to which a new MD oxidation kinetic scheme [28] is able to simulate measured droplet targets for the configuration of Fig. 1, and to offer new insights on the MD burning process for a range of conditions. The experimental conditions reported here are the following: 0.53 mm < D_o < 0.57 mm; T_∞ = room value and P_∞ = 1 atm.

The outline of the paper is as follows. Section 2 presents the experimental design. The numerical analysis is described in Sec-
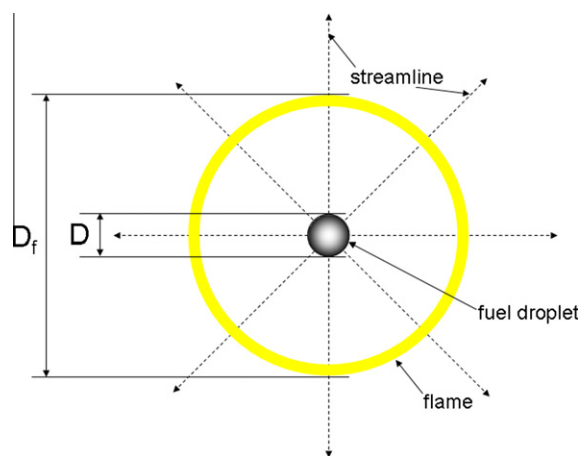

Fig. 1. Schematic of a spherically symmetric droplet flame.

tion 3. Representative images showing the droplet and flame structure are discussed as well as the experimental and numerical results are discussed in Section 4.

2. Experimental design and procedures

The experiments are carried out using a design that restricts physical motion of the droplet to produce a very small Reynolds number ($Re = \frac{U_r D}{v}$, where the relative velocity $U_r = |U_d - U_\infty|$), and under conditions where the Rayleigh number, $Ra = \frac{g\beta(T_f - T_d)D^3}{\alpha v}$, is also small as promoted by carrying out the experiments in a low gravity environment. The experiment is based on a design described previously [25,29,30] and only a brief discussion is presented here.

The experiment involves deploying isolated test droplets onto very small support fibers in a stagnant ambience in a sealed chamber, then releasing the chamber with deployed droplet and associated instrumentation into free fall. During the fall, the test droplet is ignited and the burning history is recorded. Figure 2 is a schematic of this process. The gravity level in the moving frame of reference is commensurate with the air drag around the free-fall package. A gravity level of approximately 10^{-4} of Earth's normal gravity is achieved by housing the instrumentation package in a larger chamber which is also in free fall so that the inner package falls relative to the outer package.

The droplets are deployed onto the intersection of two 14 μm diameter SiC fibers crossed at approximately 60° to prevent the droplets from sliding along the fibers while they burn. The droplets are deployed onto the fibers by directing a droplet stream from a piezoelectric generator onto the fibers, and the droplet diameter of interest is developed by successive collisions of droplets with the fiber. For the experiments reported here, the initial droplet diameters (D_o) examined are 0.53–0.57 mm.

The droplets are ignited by two sparks generated across two electrode pairs positioned on opposite sides of the droplet (though we have also ignited the test droplets by a hot wire arrangement [29]). The sparks were activated approximately 300 ms after the chamber was released into free-fall and were kept on for 800 μs. The lowest energy to the electrodes that could still ignite the droplets was employed in order to reduce the disturbance of the surrounding gas by the spark. The spark energy to ignite the drops was estimated (very approximately) based on formulations appropriate to the spark circuit employed to be on the order of 0.1 J for the particular geometrical arrangement of the electrode position and fuel of the present investigation.

The energy dissipated by the spark could influence the initial period of burning by its impact on the temperature of the gases in the immediate vicinity of the droplet. After ignition, the electrodes are immediately retracted to eliminate their influence on the thermal field surrounding the droplet. More than the spark energy, it was found that the electrode reaction process influenced the flow field by the shear-induced motion of the linear retraction [25].

Cameras provided the primary diagnostic equipment to record the droplet burning process. From this information the evolution of droplet and flame diameters are obtained. These more physical targets provide an indirect link to the combustion chemistry that more direct measurements of the evolution of species produced during the burning process could provide. The challenge of carrying out the experiments under free-fall conditions restricted the diagnostics that could be brought to bear on the droplet burning process. In particular, the evolution of the droplet combustion chemistry (e.g., distribution of species produced around the droplet) was not measured. Nonetheless, the data reported still provide a rigorous test of droplet burning models. Such an effort is further discussed in Sections 3 and 4.

A color camera was used to record the structure of the flame (Hitachi, HV-C20, 3CCD 0.3 MP/frame camera operated at 30 frames/s and a shutter speed of 1/250 s, fitted with a Nikkor 135 mm f/2.0 lens (f-stop = 2.8 is used) and two Kenko 36 mm extension tubes). A black and white (BW) camera (Canadian Photonic Labs, MS-80 K, 3.9 MP/frame camera operated at 200 frames/s and a shutter speed of 1/5000 s, fitted with a 90 mm Olympus Zuiko f/2.0 lens (f-stop = 5.6), an Olympus OM telescopic Extension Tube 65–116 mm (fixed at 100 mm) and a Vivitar MC teleconverter) provided photo-quality images of the backlit droplet. The backlighting is provided by a 1-Watt LED lamp (Black Diamond, LTD.).

A frame-by-frame analysis of the video images was used to obtain quantitative measurements of the droplet diameters using an automated MATLAB-based algorithm that loads a series of consecutive images and applies an ellipse fitting routine to the droplet boundary. Details are given in [31]. Flame diameter (D_{flame}) measurements were made with more manual input using CorelDraw 9. The procedure involved placing a digital circle on an image and adjusting its size to provide a best-fit diameter. The measurements provide dimensions of the object in pixels which were converted to millimeters with a calibration ball (a 0.79 mm diameter tungsten carbide ball bearing, Salem Specialty Ball Company) that was recorded under identical lighting conditions. It should be noted that the flame diameter measurements are far more uncertain than the droplet diameter measurements owing to the difficulty of identifying the actual boundary of the outer luminous zone. This is reflected in the uncertainty bars of the flame diameter data discussed in Section 4.2.

3. Numerical analysis

The classical theory of droplet burning [23] incorporates a number of assumptions that, ultimately, have proven in recent years to be deficient. These include assuming a quasi-steady behavior of the gas phase, constant properties, negligible radiation, a single step reaction at the flame, and no soot formation. Nonetheless, the classical result still qualitatively (but not quantitatively) predicts the physics of the process for some elements of the burning process, for example that burning rates qualitatively scale inversely with liquid density.

Comprehensive numerical treatments of the base case of Fig. 1 have been presented that extend considerably the classical assump-
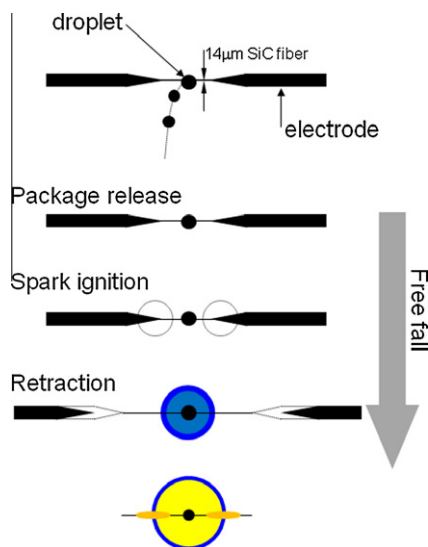

Fig. 2. Illustration of the sequence of droplet deployment, package release, spark ignition, retraction of the spark electrodes for the experiment.

tions and provide for a higher degree of fidelity when compared with experiment. For example, Cuoci et al. [32] used a finite volume approach to solve the governing equations of mass, momentum, species and energy with gray-gas radiative effects. Kroenlein [33] used the conservation equations in integral form along with sub-models for the combustion kinetics, non-luminous radiation and a detailed methodology to predict thermophysical properties to simulate the burning process of methanol and ethanol droplets.

Methanol droplet combustion has been modeled including conditions to promote extinction and the mechanisms associated with the influence of support fibers on the droplet burning process by Farouk and Dryer [26,34]. In the present investigation, we adopt this approach to model combustion of MD droplets and compare the results with the experiments described previously. For the sake of completeness a brief description of the model is provided here. The model considered here assumes local thermodynamic equilib-

rium and low Mach number. Species and energy conservation equations for the control volumes in both phases are:

$$\int_{r_-}^{r_+} \frac{\partial(y_i\rho)}{\partial t}r^2 dr + \frac{r^2\dot{r}|_{r_-}^{r_+}}{\frac{1}{3}r^3|_{r_-}^{r_+}} \int_{r_-}^{r_+} y_i\rho r^2 dr + y_i(\rho u - \rho\dot{r})r^2\big|_{r_-}^{r_+}$$
$$= -y_i\rho V_i r^2\big|_{r_-}^{r_+} + \int_{r_-}^{r_+} \dot{\omega}_i r^2 dr \tag{1}$$

$$\int_{r_-}^{r_+} \frac{\partial(h\rho)}{\partial t}r^2 dr + \frac{r^2\dot{r}|_{r_-}^{r_+}}{\frac{1}{3}r^3|_{r_-}^{r_+}} \int_{r_-}^{r_+} h\rho r^2 dr + h(\rho u - \rho\dot{r})r^2\big|_{r_-}^{r_+}$$
$$= -q r^2\big|_{r_-}^{r_+} + S_{loss/gain\,due\,to\,fiber} \tag{2}$$
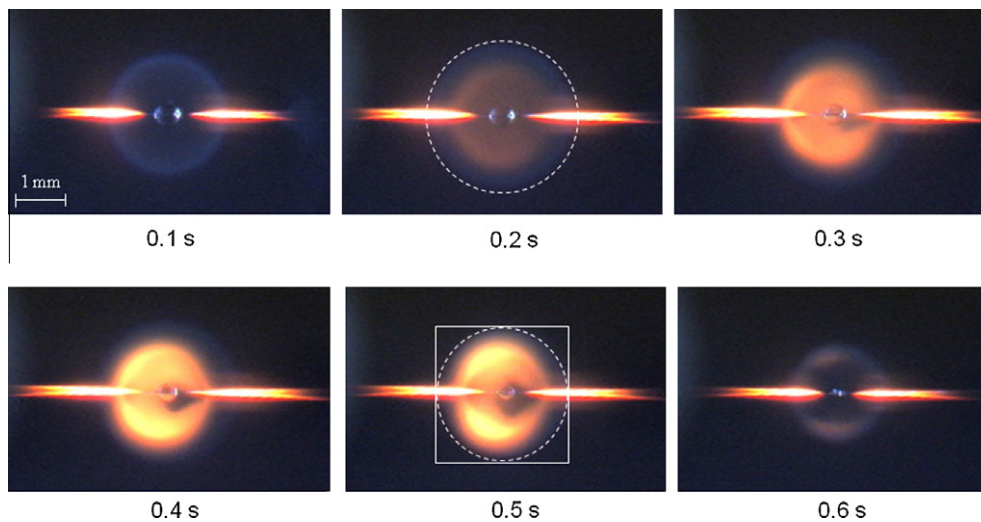
$$\sum_{\forall i} y_i = 1 \tag{3}$$

Fig. 3. Color images showing evolution of MD droplet flame. The initial diameter D_o of this particular experiment is 0.56 mm (dotted line show how flames' diameter (as an equivalent ellipse) was determined; outer luminous (blue) zone was used for flame boundary). (For interpretation of the references to color in this figure legend, the reader is referred to the web version of this article.)
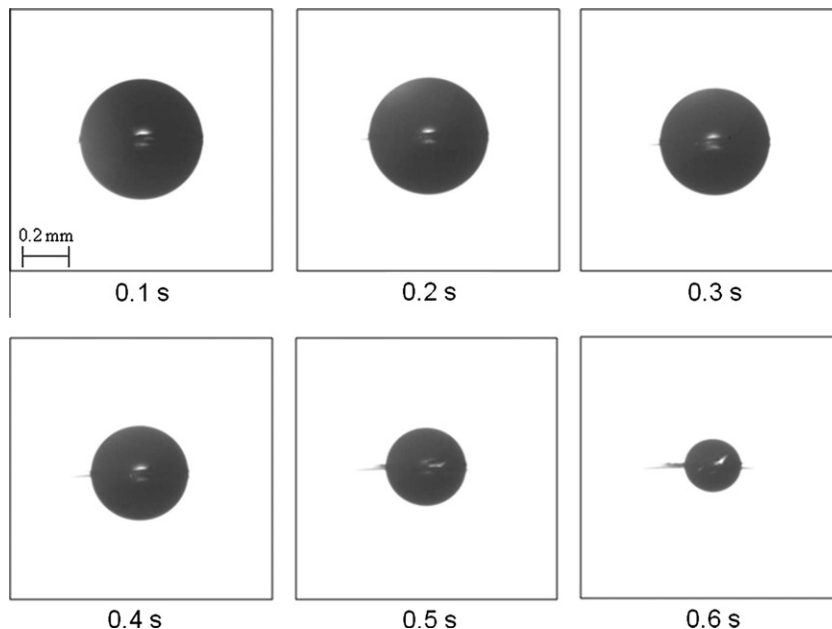

Fig. 4. Back-lit images of the droplet (the black object) obtained by the BW high speed camera during the combustion process. The initial diameter of the droplet is $D_o = 0.56$ mm.
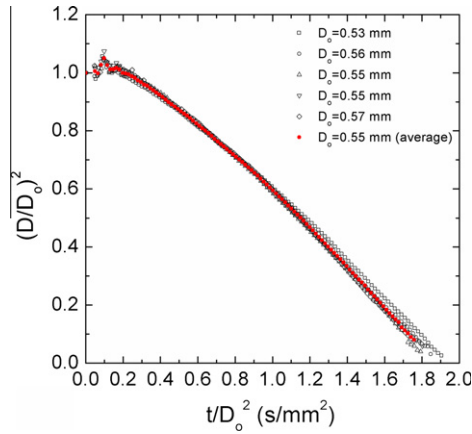
Fig. 5. Evolution of droplet diameters for MD combustion. Black (open symbol) data are the original five individual experiments and the red (closed symbol) data are the averaged values from the five runs. (For interpretation of the references to color in this figure legend, the reader is referred to the web version of this article.)
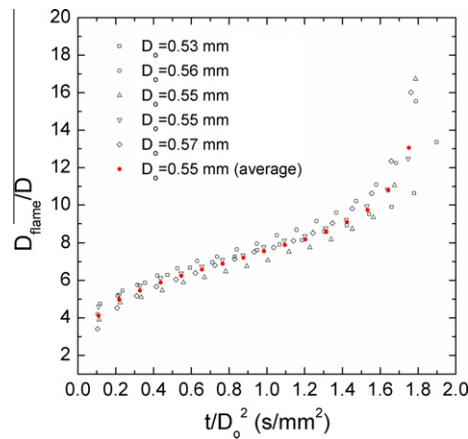

Fig. 6. Flame standoff ratios (FSR = D_{flame}/D) of MD droplet flames. Black (open symbol) data are from five individual runs and red (closed symbol) data are the averaged values from the five runs. (For interpretation of the references to color in this figure legend, the reader is referred to the web version of this article.)

where y_i = mass fraction, ρ = mass density, r = radius, u = bulk fluid velocity, $\dot{r}$ = velocity of the control volume boundary, V_i = diffusion velocity, $\dot{\omega}_i$ = rate of species production due to chemical reaction, h = enthalpy per unit mass and q = heat flux. The heat flux q represents here a lumped term, with contributions from chemical enthalpy of diffusing species, thermal conductive heat transport, radiative heat transport and the Dufour effect. $S_{loss/gain\ due\ to\ fiber}$ is the loss and gain due to the presence of the tether fiber.

Equations at the liquid–gas interface arise either through satisfaction of thermodynamic constraints or conservation of material fluxes:

$$y_i(\rho u - \rho \dot{r})|_-^+ = -y_i \rho V_i|_-^+ \quad (4)$$

$$\sum_{i \in liquid} h_{vap,i}[y_i(\rho u - \rho \dot{r}) + y_i \rho V_i]_+ = -q|_-^+ - q_{fiber} \quad (5)$$

$$\sum_{i \in gas} y_{i,+} = 1, \quad \sum_{i \in liquid} y_{i,-} = 1, \quad \text{and} \quad T_+ = T_- \quad (6)$$

$$x_{i,+} p = x_{i,-} \gamma_i(T, x_{j,-}) p_{vap,i}(T) \quad (7)$$

where $h_{vap,i}$ = enthalpy of vaporization, p = system pressure, T = temperature, x_i = mole fraction, γ_i = activity coefficient and $p_{vap,}$

$_i$ = vapor pressure of the ith component in its pure state. The symbols '+' and '−' denote location in the gas and liquid phase, respectively. The heat flux q at the interface has contribution from chemical enthalpy of diffusing species, thermal conductive heat transport, radiative heat transport and Dufour effect. The q_{fiber} represents the heat flux through a tethering fiber at the interface.

As the droplets are supported by fibers, a model for heat transfer through the fiber previously developed [26,34] was also incorporated into the numerical analysis to assess the effect of the fiber on the predicted results. Heat transfer through the tether is analyzed by a model that assumes a one dimensional thermal system (justified on the basis of the Biot number (based on fiber radius) being very small) with conductive heat transfer in the solid phase of the fiber and radiative transfer and convective heat transfer interactions with the surrounding gas phase. The convective heat transfer on the fiber surface is modeled by using a Nusselt number correlation associated with the local Stefan flux, and feeds into the main domain in every time step (see [34] for details). Although some literature has already experimentally shown that the effect of SiC fibers on the droplet burning process can be insignificant [25], effects of fiber sizes, thermal conductivities and Nusselt numbers associated with heat transfer through the fiber were nonetheless incorporated in the model to assess the potential influence of these parameters.

The model as formulated and executed here amounts to a detailed numerical simulation of the burning process for the configuration of Fig. 1, which is currently the only liquid fuel burning process that is amenable to this level of numerical detail and precision. The main adaptation of the present study is to incorporate the combustion kinetics of MD described in [28], and to use physical properties in the simulation that are appropriate to MD. The combustion kinetics of MD used in the current investigation have been compared and validated against experimental results from shock tube, jet-stirred reactor, and counterflow burner [28]. This study further incorporates some multi-phase aspects into the previously developed gas phase oxidation schemes to approach the droplet burning problem. The combustion chemistry incorporates 238 species and 1244 reaction mechanisms. As such, 238 individual species conservation equations are solved simultaneously along with detailed formulations for radiative transfer and physical property correlations. Since MD droplets only produce a minimal amount of soot and no soot shell structure for the range of droplet sizes investigated here (see Section 4.1), this influence was not considered in the model.

In the numerical analysis, the volume boundaries for liquid and gas phase are deliberately defined to coincide with the liquid–gas interface. The gas phase domain is 200 times larger than the initial droplet size and the outer boundary of it (far field) is constrained by Dirichlet conditions (constant ambient composition N_2/O_2 = 0.79/0.21 and T = 298 K).

Spark ignition is simulated by introducing a spherically symmetric high temperature region of trapezoidal shape with a peak temperature of 2000 K located at the side of the droplet. The total ignition energy used in the simulations is 1.1 J, which is also the lowest possible energy that numerically triggered an ignition.

4. Results and discussions

4.1. Droplet flame configuration

Selected color and BW images of MD droplets are shown in Figs. 3 and 4, respectively. The spherical flame shapes are maintained throughout burning. The two needle-like glows in Fig. 3 are due to the interaction between flame and fibers. The box and circle superimposed on the images at 0.2 s and 0.5 s indicate the
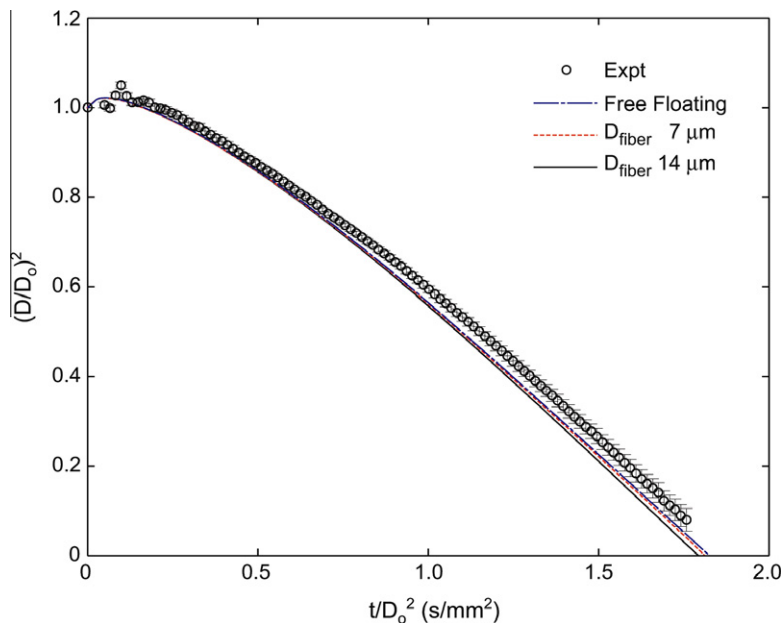
Fig. 7. Evolution of averaged droplet diameters over the combustion process (the error bars show the standard deviations of the averaged data) – compared with simulations of free floating droplet and with various fiber diameters D_{fiber} (k_{fiber} = 5.2 W/mK and Nu = 0.36).
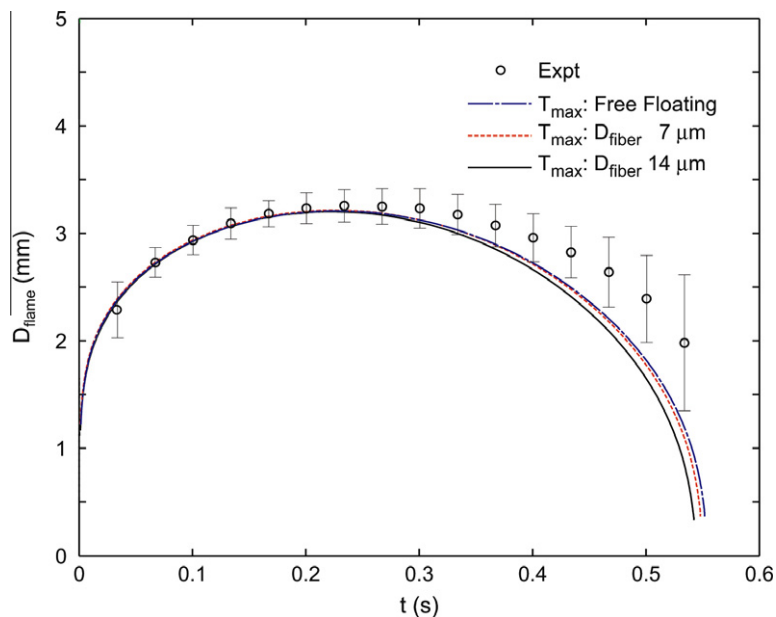

Fig. 8. Flame diameter evolution: experiments (the error bars show the standard deviations of the averaged data) vs. simulation with various fiber sizes (k_{fiber} = 5.2 W/mK and Nu = 0.36).

means by which the flame diameters were determined as briefly discussed in Section 2. As shown in Fig. 3, the flame color is almost entirely blue until an inner yellow core is established after 0.1 s which then slightly alters the asymmetry of the inner core.

Figure 4 shows a selected set of backlit images that illustrate the evolution of the droplet (the black object) during the burning process. As can be seen, the droplet boundary is fairly sharp. The presence of the fiber does not seem to affect the droplet geometry as the droplet remains nearly spherical (or circular on the 2-D plane), except very near the end of the burning process.

Most obvious in Fig. 4 is the absence of a soot shell, indicating that MD does not produce enough soot to form a shell structure for the range of initial droplet diameters investigated here. The

precise mechanisms for the lack of soot formation for the combustion of methyl ester molecules do not appear to be well understood [17]. One perspective is that the C–O bonds in the oxygenated molecule remain intact during the ignition process so that there are fewer C atoms available to make soot after ignition [35]. However, if the oxygen produces CO_2 (which it apparently will for MD [10]) the bonded oxygen in the ester may not be as effective to reduce soot formation.

4.2. Quantitative data

Measurements of the droplet diameter (D) obtained from images like those shown in Fig. 4 are normalized with the initial
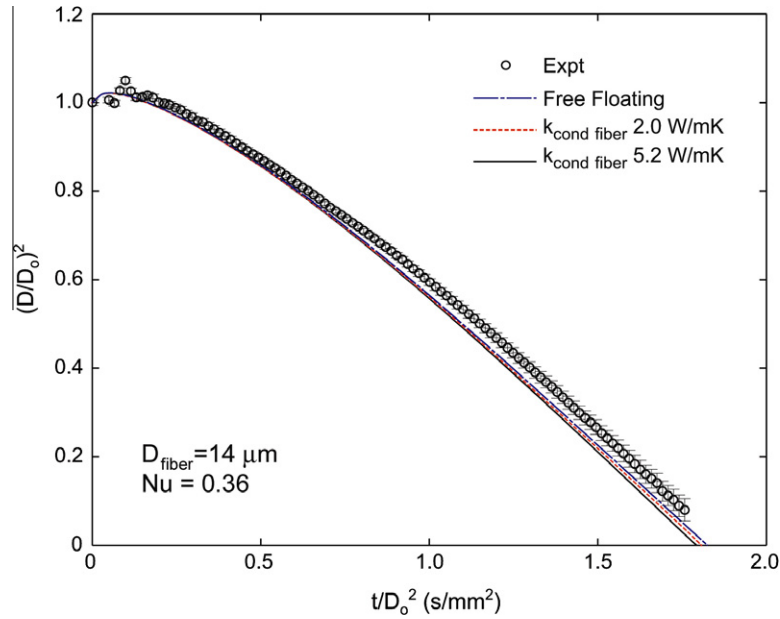
Fig. 9. Evolution of averaged droplet diameters over the combustion process – compared with simulations of free floating droplet and with various thermal conductivities for the fiber k_{fiber} (the error bars show the standard deviations of the averaged experimental data). D_{fiber} = 14 μm and Nu = 0.36.
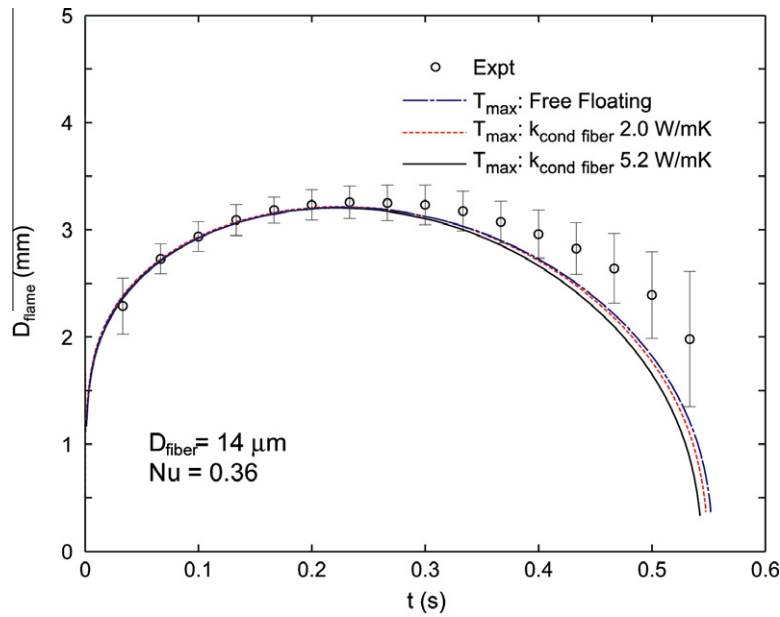

Fig. 10. Flame diameter evolution: simulation performed with free floating (no fiber) condition and with different thermal conductivity for the fiber. D_{fiber} = 14 μm and Nu = 0.36.

diameter (D_o) and presented in Fig. 5 using the coordinates suggested by the classical droplet combustion theory [23],

$$\left(\frac{D}{D_o}\right)^2 = 1 - K\frac{t}{D_o^2} \qquad (8)$$

where t is time (s) and K is the burning rate (mm^2/s). Data from five repetitions are shown along with the average of these runs. The measurements show good repeatability.

There are two aspects of the data in Fig. 5 not part of the classical theory: the initial period in which the droplet swells as its density drops due to being heated by the surrounding hot gases from the flame; and the slight curvature of the evolution of droplet

diameter which indicates a time dependent burning rate ($K(t)$). In the early period, the droplet heats faster than the fuel evaporates to give the swelling effect. The data are more scattered in this period due to the disturbance attributed to the physical impact of the spark ignition on the droplet. After this initial period, the predicted (and measured) evolution of droplet diameter shows some slight curvature which may be due to unsteady heating that persists throughout burning.

The evolution of flame diameter as extracted from the color images (cf. Fig. 3) is shown in Fig. 6, presented as the relative position of the flame boundary to the droplet boundary (flame standoff ratio, FSR $\equiv D_{flame}/D$). The trends are again significantly different from the classical theory [23] that predicts D_{flame}/D to be constant.
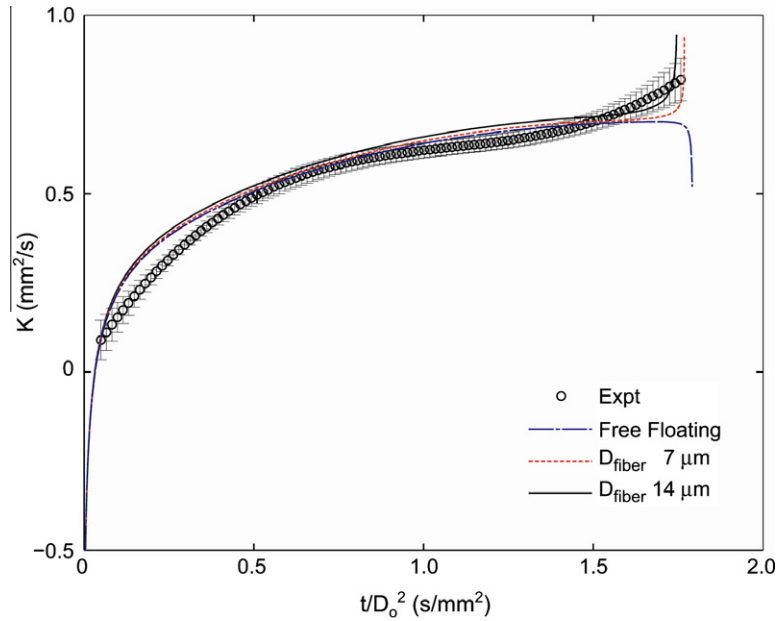
Fig. 11. Burning rate evolution: experiments (with error bars showing the standard deviations) vs. simulation with different fiber sizes D_{fiber}. (k_{fiber} = 5.2 W/mK and Nu = 0.36).
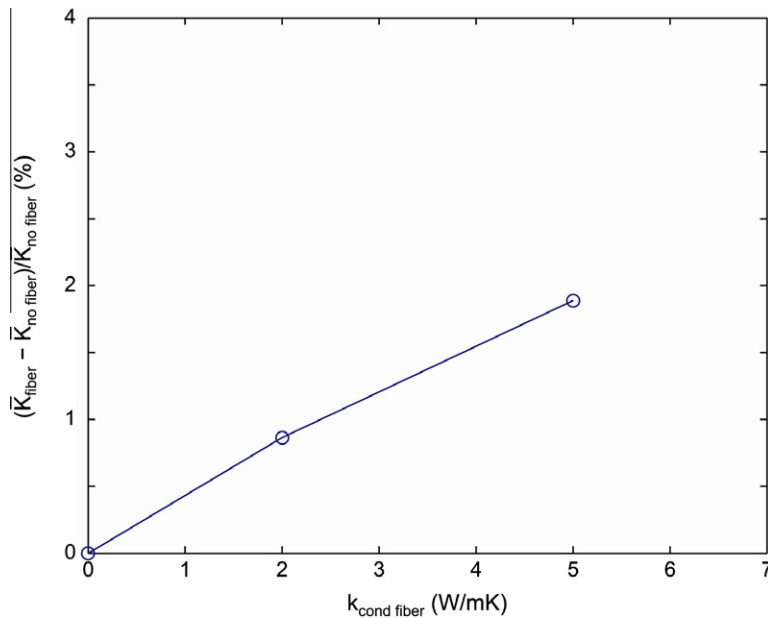

Fig. 12. Numerical results of deviation in burning rate K with various thermal conductivities for the fiber k_{fiber}. (D_{fiber} = 14 μm and Nu = 0.36).

Due to the lower resolution (0.3 MP/frame) of the color camera and greater difficulty of identifying the flame boundary (taken as the outer luminous zone as discerned manually), there are fewer flame diameter data, and with larger uncertainty, compared to the droplet diameter measurements (Fig. 5).

4.3. Comparison of measurements with numerical simulation

The results predicted using the comprehensive droplet combustion model outlined in Section 3 are compared with the data discussed in Section 4.1 and then used to simulate additional conditions to provide new insights into the MD droplet burning process. The comparisons with the measurements include the evolution of droplet and flame diameter.

Figure 7 compares the simulated evolution of droplet diameter with the experimental values. The standard deviations (vertical bars) pertaining to each averaged data point (black open circle) are calculated from the data for the five individual experiments of Fig. 5. Numerical results are shown for three different fiber sizes: D_{fiber} = 14 μm; D_{fiber} = 7 μm; and D_{fiber} = 0 ("free floating", where the droplet is not supported by any fiber structure (blue line)).

As shown in Fig. 7, the three numerical results with various fiber conditions are extremely close to one another, with the free floating prediction being closest to the experimental data. This suggests that fibers with such small diameters are not a significant factor to affect the droplet burning history until the very end of burning where the fiber size becomes relatively large compared to the droplet size. Numerical results are very close to the lower
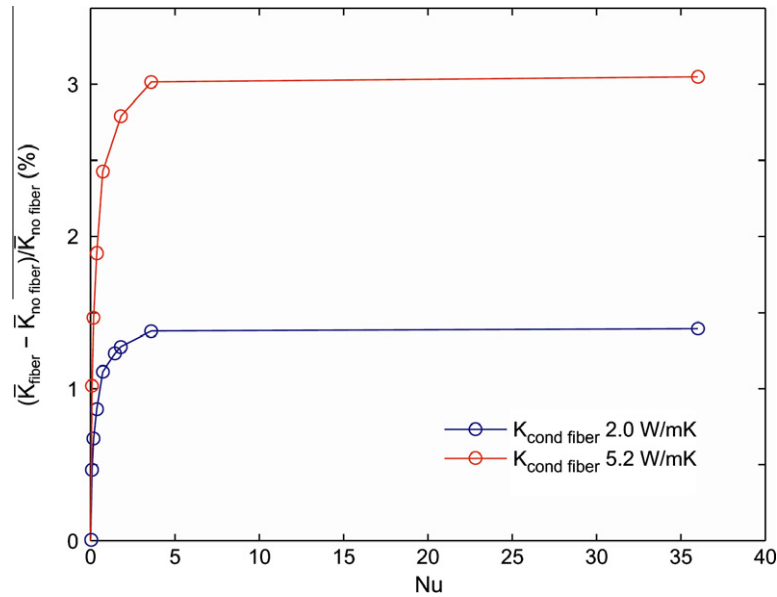
Fig. 13. Effect of Nusselt number on the burning rate K with various thermal conductivities for the fiber (D_{fiber} = 14 μm).

limit of the error bars of experimental data though there is still some visible difference at the end of burning. This difference might be caused either by the determination of ignition time for both experimental and numerical cases, by the ignition energy used as the spark energy in the experiments could not be accurately measured and provided for the simulation, or the greater difficulty in obtaining accurate measurements for the small diameters at the end of burning. However, the final slopes of the predicted burning curve in Fig. 7 appear to be consistent with the experimental values.

In the quasi-steady period of burning (the approximate range 0.75 s/mm^2 < t/D_o^2 < 1.25 s/mm^2) the simulated droplet diameter is slightly smaller than the measured diameter. This difference could be due to the influence of spark energy on the temperature field at the moment of ignition. Employing a larger spark energy in the experiments could reduce the unsteady heating period so that regression begins at an earlier time and shifts the time scale of the experiments to slightly shorter times for a given droplet size.

Figure 8 compares the numerically predicted flame diameters (D_{flame}), defined as the radial position of maximum temperature in the 1-D simulation domain, for several fiber diameters with the experimental data. The numerical results for various fiber sizes do not differ until 0.3 s into the burn. Clear differences are observed thereafter to the end of combustion where the free floating droplet (D_{fiber} = 0) has a slightly larger flame diameter and the flame diameter for D_{fiber} = 14 μm has the smallest flame at the same time. Nonetheless, trends are very consistent with the maximum D_{flame} occurring at 0.22 s for the three simulated fiber diameters and generally show a very good agreement with the measurements.

The results for the larger fiber (14 μm) show a slightly larger burning rate (cf. Fig. 7) due to the extra source for heat transfer through the fiber, causing the measured D_{flame} to drop earlier at the end of burning. Compared to the experimental data, the general trends are nonetheless very close, with the maximum D_{flame} occurring at 0.22 s. However, at the end of burning the predicted
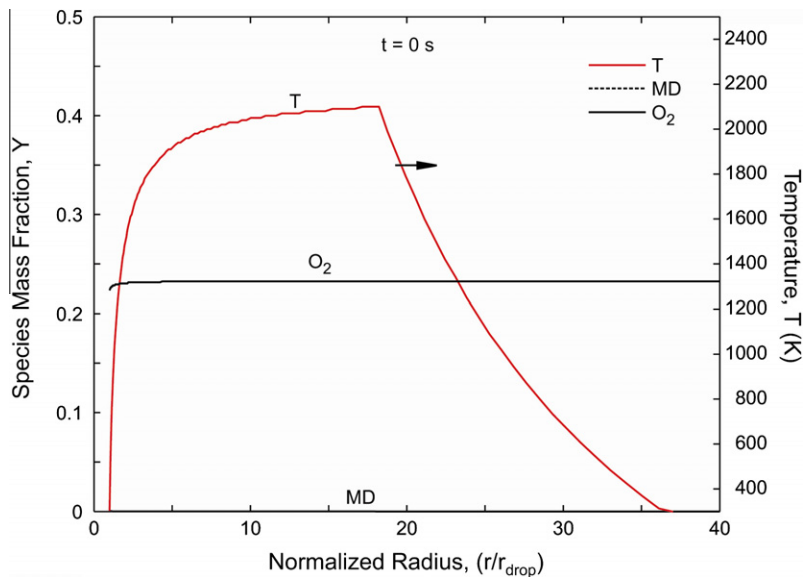

Fig. 14. Initial profiles (t = 0 s) of temperature and concentrations of MD and O_2. (D_{fiber} = 14 μm, k_{fiber} = 5.2 W/mK and Nu = 0.36).

D_{flame} is significantly lower than the averaged experimental data. The large error bars on experimental shown in Fig. 8 reflect the lower resolution of the color images and thus a greater challenge to obtain accurate D_{flame} at the end of burning. The lower end of the error bar at the very end of burning is nonetheless close to the predicted data.

The influence of fiber thermal conductivity, k_{fiber}, on droplet burning will depend on the specific values considered. The thermal conductivity of the SiC fibers employed in the present experimental effort was not measured directly. The literature shows a strong temperature dependence, ranging for bulk SiC from several hundred W/mK at room temperature down to 30 K at 1500 K [36]. Fibrous SiC strands of 20 μm diameter have conductivity values of about 5 W/mK [37]. Comparisons of droplet burning using other fiber materials (i.e., a ceramic fiber) with a known thermal conductivity (i.e., $k_{fiber} \sim 2$ W/mK [38]) suggests that the lower limits of fiber thermal conductivity may be more relevant to the SiC

fibers employed in the present experiments. In this section simulations are reported using k_{fiber} = 2 W/mK and 5.2 W/mK.

Figure 9 shows the evolution of droplet diameter for a given D_{fiber}. For 2.0 W/mK < k_{fiber} < 5.2 W/mK the results are not substantively affected by the fiber for k_{fiber} in this range. At the end of burning, it still can be seen that the fiber with higher thermal conductivity starts to act as an extra heat transfer path for the flame to transmit heat into the droplet causing the droplet size to decrease slightly more quickly, but the effect is minimal.

The influence of k_{fiber} on predicted D_{flame} is presented in Fig. 10. Again, the change of k_{fiber} within the range 2.0 W/mK < k_{fiber} < 5.2 W/mK does not appear to strongly affect D_{flame}. The simulation with higher k_{fiber} is consistent with the trend for increasing the fiber diameter as both variations promote heat flow through the fiber thereby increasing the burning rate and reducing D_{flame} slightly more quickly. The free-floating limit shows deviations from the fiber-supported predictions for $t > 0.3$ s where the difference be-
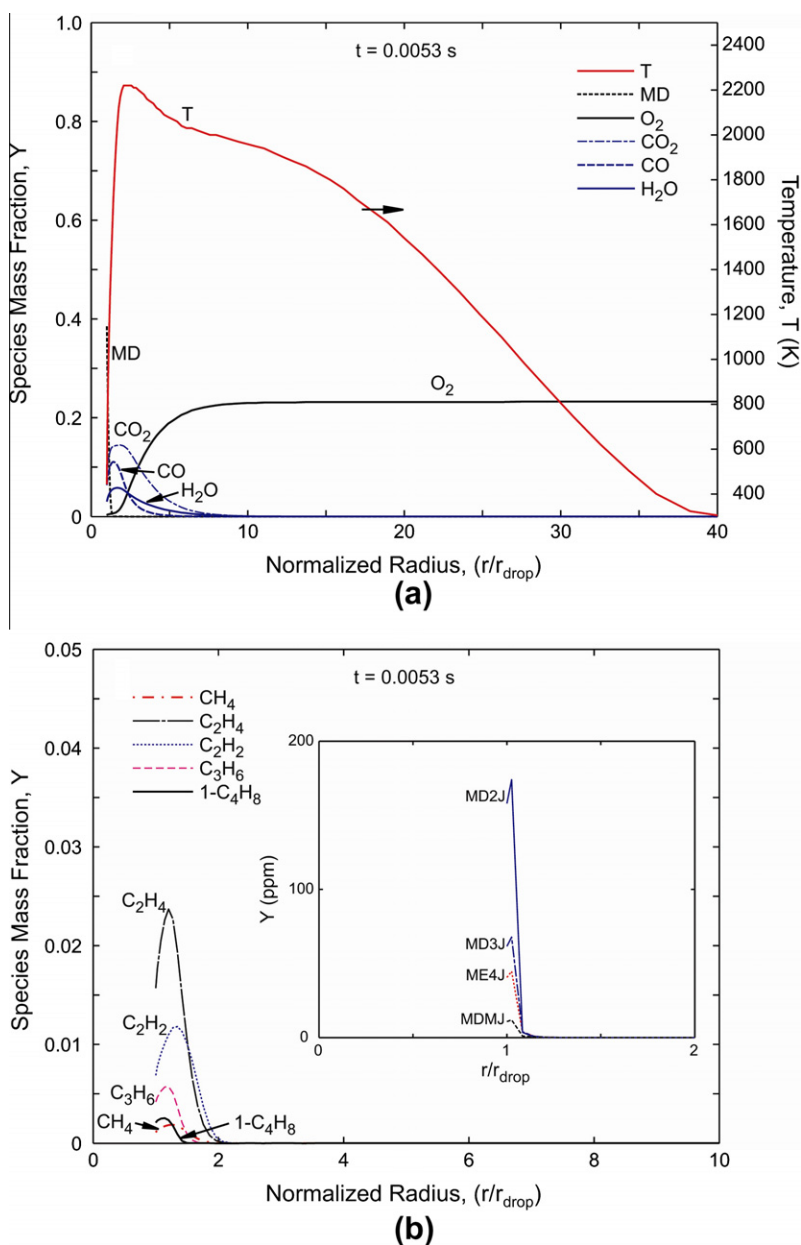

Fig. 15. Spatio-temporal profile of species and temperature at 0.0053 s. (a) Profiles for temperature T and mass fraction Y of main reactant (MD and O_2) and products (CO_2, CO, and H_2O) and (b) important intermediates (CH_4, C_2H_4, C_2H_2, C_3H_8, and 1-C_4H_8). (D_{fiber} = 14 μm, k_{fiber} = 5.2 W/m K and Nu = 0.36).

tween numerical and experimental results becomes significant at the end of burning.

A comparison of the burning rates is a more stringent test because differentiation amplifies uncertainties in the evolution of droplet diameter. For the data shown, the original droplet diameter data (Fig. 5) were smoothed with a 4th order polynomial and the first derivative was then taken to determine the burning rate from the averaged data. It is important to note that the order of polynomial fit will affect the derivative value. Trends could emerge that are artifacts of the order of the polynomial used to fit the data. With this fact in mind, the simulated burning rates for the free floating and fiber-supported conditions ($D_{fiber} = 0$ μm, 7 μm and 14 μm) are shown in Fig. 11.

The experimental burning rates increase with time, with the increase being significant in the early period of burning, followed by a more gradual (i.e., quasi-steady) period in the mid region of burning (i.e., 0.5 s/mm$^2 < t/D_o^2 < 1.5$ s/mm^2) where the average K is

about 0.6 mm^2/s. At the very end of burning, $t/D_o^2 > 1.7$ s/mm^2, K shows a noticeable increase which is suggestive of an extinction-like process. However, as noted above regarding the order of polynomial fit to determine burning rate, the increase of K at the end of burning in Fig. 11 could well be an artifact of the order of the polynomial fit to the data in Fig. 5. At the same time, the increase is consistent with an ever increasing influence of the fiber on the burning rate. As the droplet size decreases D_{fiber} remains the same, so there must always be some influence of the fiber even for arbitrarily small fiber sizes.

As shown in Fig. 11, numerically predicted burning rates increase from a negative value beginning with the initial droplet heating period associated with thermally induced expansion of the droplet, and then level off at about $t/D_o^2 \sim 0.5$ s/mm^2. The measured burning rates do not increase as substantially after ignition. However, this trend is influenced by the order of polynomial fit to the data of Fig. 5. As the simulated burning rate increases
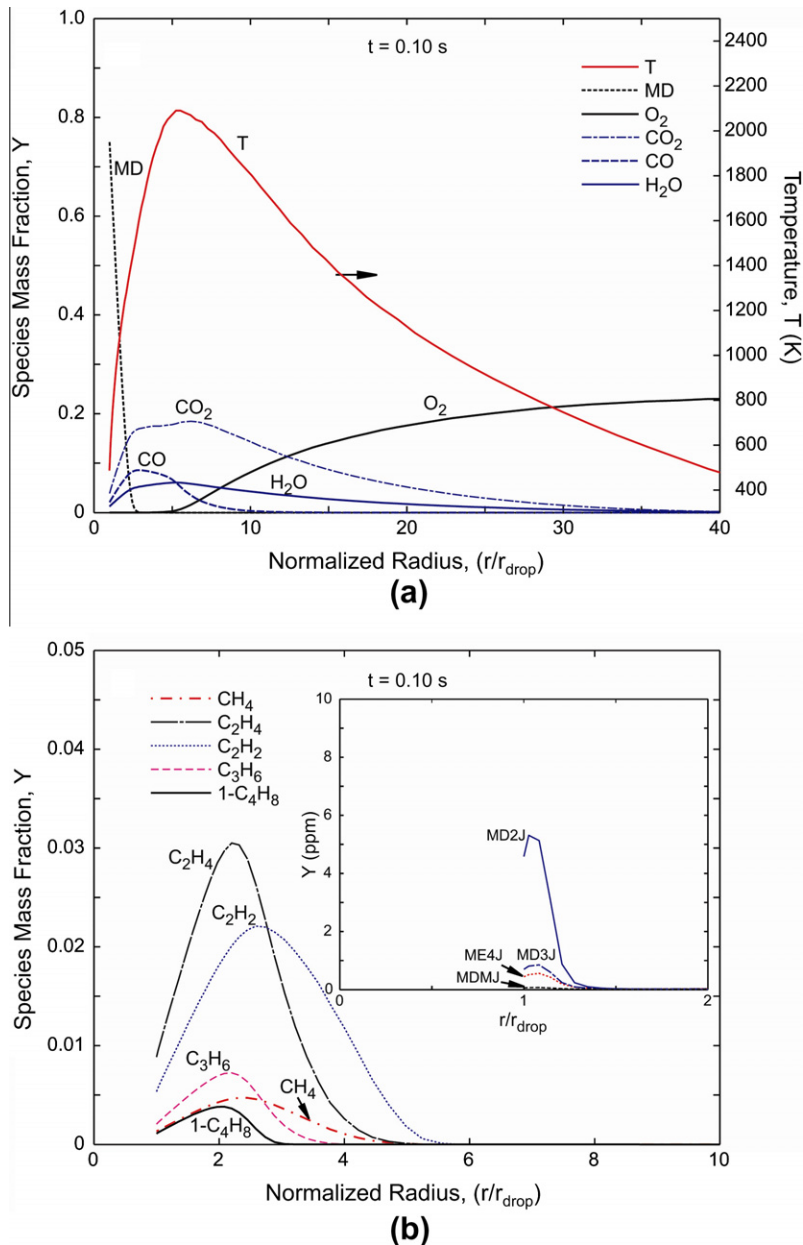

Fig. 16. Spatio-temporal profile of species and temperature at 0.10 s. (a) Profiles for temperature T and mass fraction Y of main reactant (MD and O_2) and products (CO_2, CO, and H_2O) and (b) important intermediates (CH_4, C_2H_4, C_2H_2, C_3H_8, and 1-C_4H_8). ($D_{fiber} = 14$ μm, $k_{fiber} = 5.2$ W/mK and Nu = 0.36).

more quickly than the measured rate in the early period, the extra enthalpy input to the droplet in the simulation might be slightly larger than what is actually transported in the experiments. Unfortunately, the spark energy used in the numerical simulation is the lowest possible energy to trigger ignition for MD combustion. For $t/D_o^2 > 0.5$ s/mm², the predicted burning rates agree quite well with the measurements. The simulated burning rate for a fiber-supported droplet is slightly larger than the free floating ($D_{fiber} = 0$) limit due to increased heat transport to the droplet associated with the larger fiber diameter.

To further clarify the influence of fiber thermal conductivity on burning, Fig. 12 shows the variation of the ratio of the averaged burning rate to the free-floating limit with fiber thermal conductivity. As expected, the relative burning rate increases with increasing k_{fiber}, though for $k_{fiber} = 5$ W/mK the average burning rate deviates from the free-floating limit by only 1.7%, showing that the fiber does not have a significant influence on the burning rate.

From an experimental perspective, a fiber-supported droplet combustion experiment is far easier to perform than a free-floating droplet combustion experiment because the fiber physically anchors the droplet to a fixed position relative to the imaging optics throughout burning. When the fiber has a minimal effect on the combustion process as outlined here, the results are useful for producing data that simulate the ideal configuration of Fig. 1.

The model for heat transfer through the fiber incorporated in the detailed simulation used here requires that the heat transfer coefficient (or Nusselt number) be known to account for convective transport between the tether fiber and surrounding fluid. To show the effect, Fig. 13 shows the effect of varying Nu over a wide range on the burning rate relative to the free-floating value. The lower value is the conduction limit, Nu = 0.36 and results for two values of k_{fiber} are shown. As the Nusselt number increases, the burning rate increases due to increased heat transfer from the vapor phase to the tether and levels off above Nu ∼ 4 where there is no longer

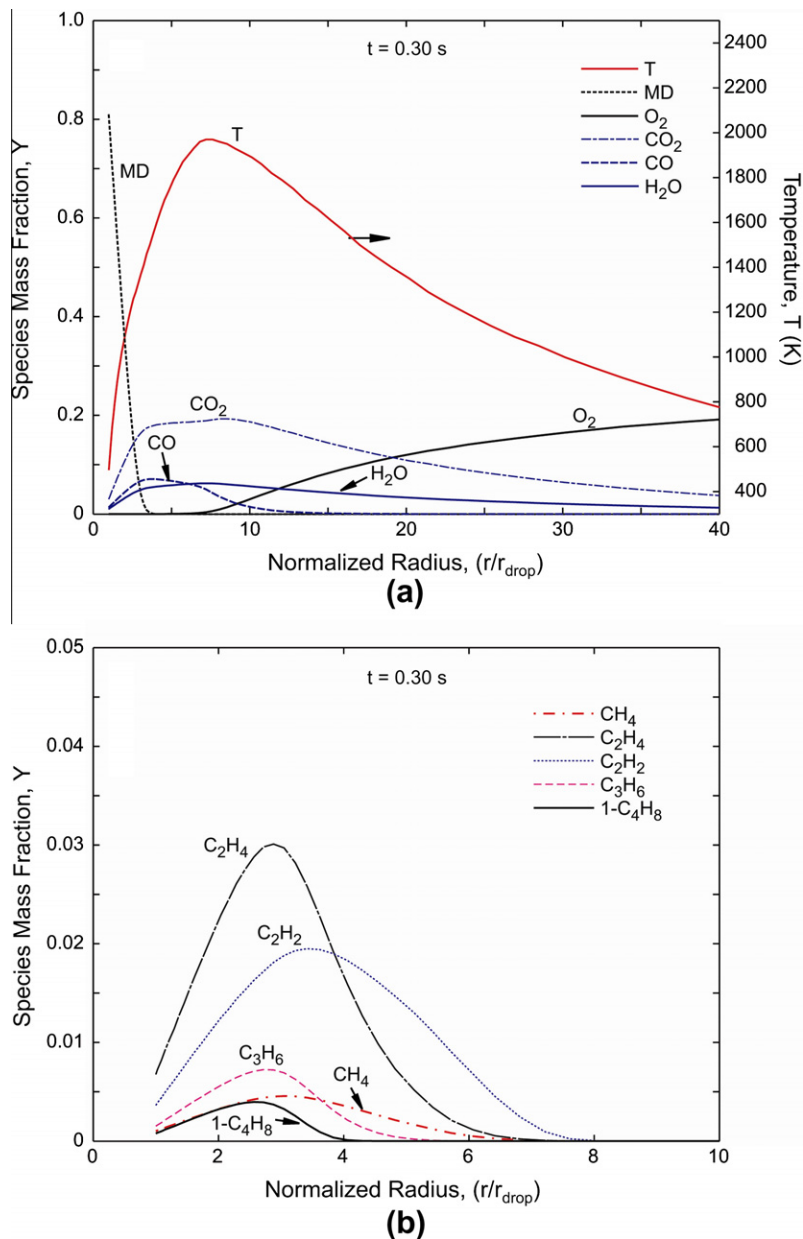**Fig. 17.** Spatio-temporal profile of species and temperature at 0.30 s. (a) Profiles for temperature T and mass fraction Y of main reactant (MD and O_2) and products (CO_2, CO, and H_2O) and (b) important intermediates (CH_4, C_2H_4, C_2H_2, C_3H_8, and $1\text{-}C_4H_8$). ($D_{fiber} = 14$ μm, $k_{fiber} = 5.2$ W/mK and Nu = 0.36).

an influence of convection. In the high Nu limit, the convective resistance is small and the vapor temperature around the fiber is close to the fiber temperature. In this case, convection (or radiation) has little influence on heat transfer through the fiber while the fiber is at its maximum temperature.

Figure 13 also shows that k_{fiber} does not have a strong influence on the burning rate for the two values simulated regardless of the strength of convection: 3% for k_{fiber} = 5 W/mK and 1.4% for k_{fiber} = 2 W/mK. An influence at this level would be difficult to discern from the experiments of burning rate (Fig. 11) that are determined by differentiating a polynomial fit to the data (e.g., Fig. 5).

4.4. Spatio-temporal evolution of species and temperature

In this section we use the numerical model to gain further insights into the MD droplet burning process. Specifically, simulations for product species and temperature distributions are presented to give further insights on the combustion chemistry employed in the simulations.

Figure 14 shows the computed temperature distribution and concentration of MD and oxygen at the ignition point (t = 0 s) from the droplet surface to the far field. Along the radial direction, the vapor temperature jumps from room temperature to around 2000 K and reaches the maximum value at $r/r_{drop} \sim 18$ (where $r = D/2$) then drops to room temperature again at $r/r_{drop} \sim 37$. The MD concentration is almost zero in the vapor phase and the oxygen level is about 0.225 (mass fraction).

Figure 15 shows the temperature distribution and the concentration for major species produced at t = 0.0053 s. The peak temperature (Fig. 15a) is around 2200 K and the droplet temperature (r/r_{drop} = 1) is still slightly lower than its boiling point (497 K) which is evidence for transient droplet heating. The concentration for MD drops dramatically along the radial direction and the oxygen level is maintained as the same as the ambience for $r/r_{drop} > 10$.
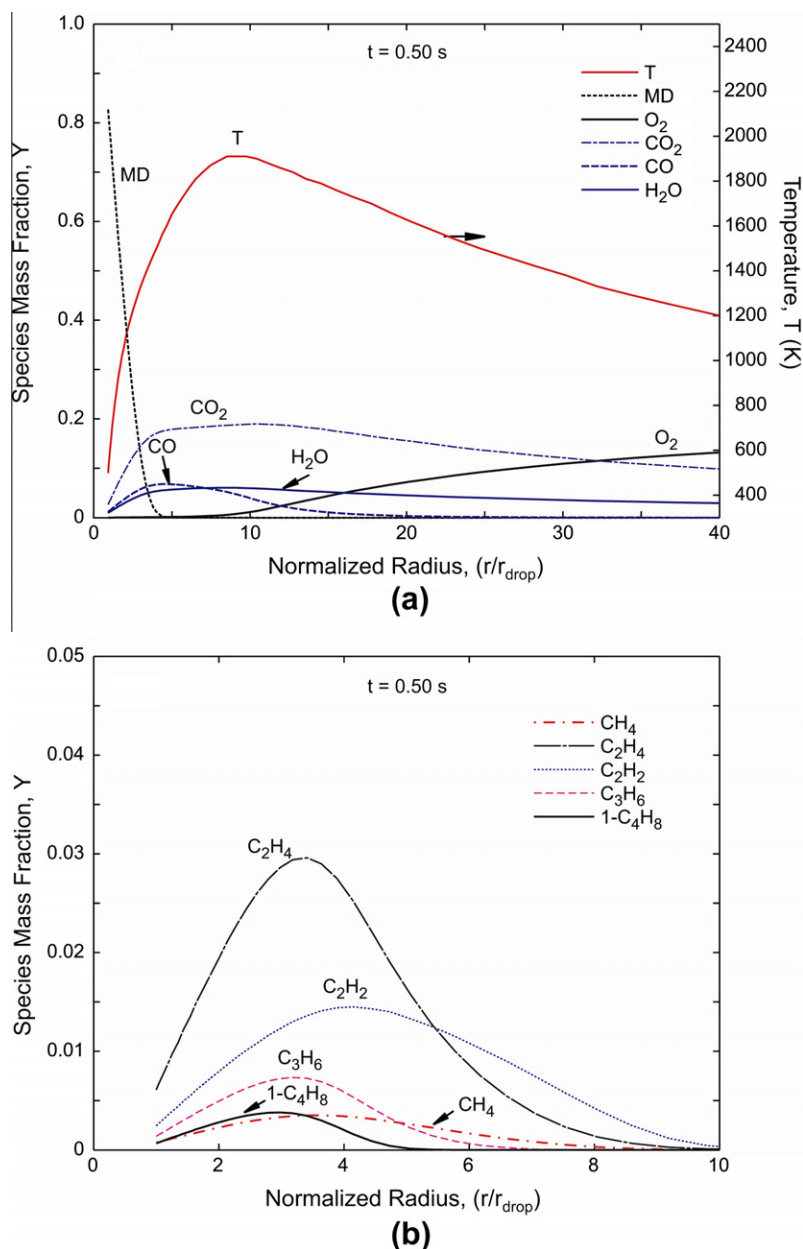

Fig. 18. Spatio-temporal profile of species and temperature at 0.50 s. (a) Profiles for temperature T and mass fraction Y of main reactant (MD and O_2) and products (CO_2, CO, and H_2O) and (b) important intermediates (CH_4, C_2H_4, C_2H_2, C_3H_8, and 1-C_4H_8). (D_{fiber} = 14 μm, k_{fiber} = 5.2 W/mK and Nu = 0.36).

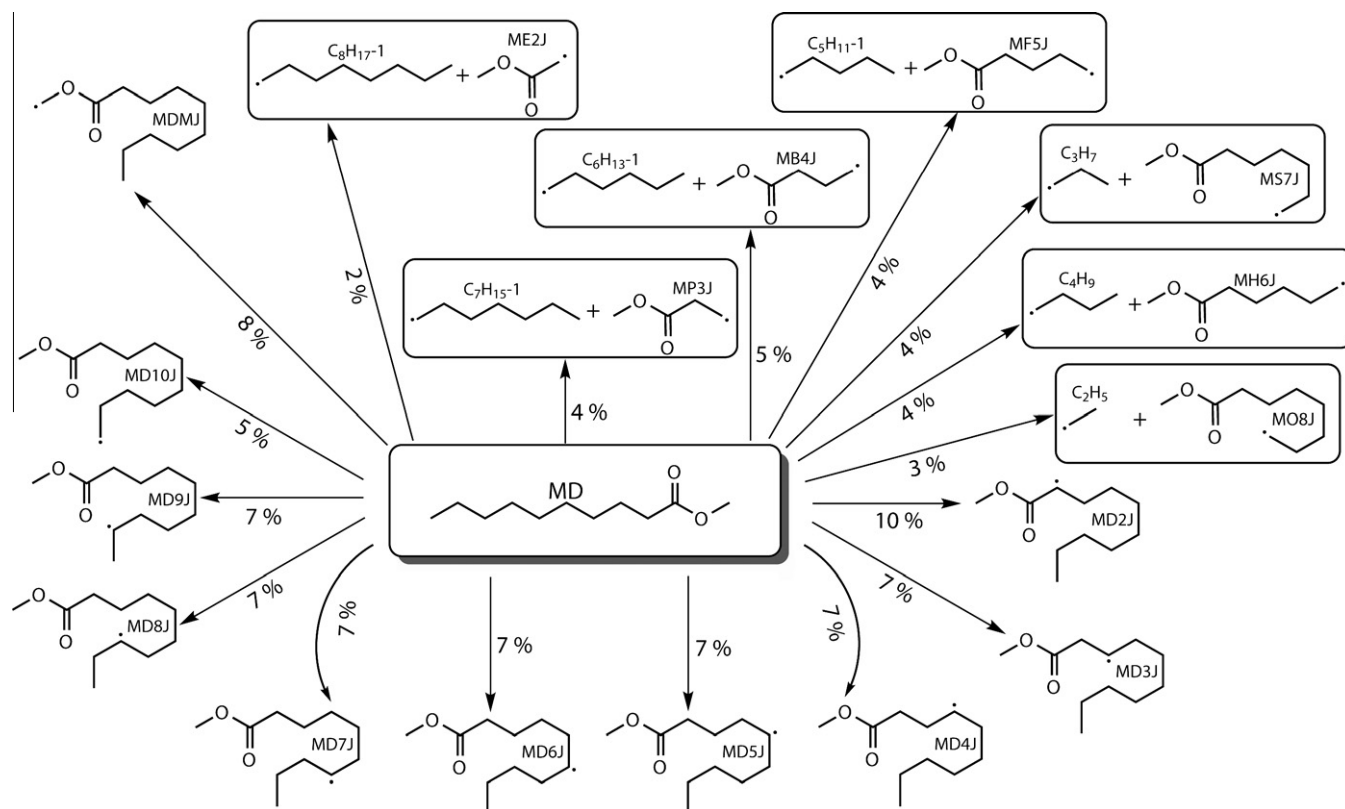**Fig. 19.** Path flux analysis of MD at the flame location during quasi-steady burning ($\Phi = 1$, $T = 1900$ K). ($D_{fiber} = 14$ µm, $k_{fiber} = 5.2$ W/mK and Nu = 0.36).

Concentrations for all the species shown in Fig. 15a only exist within $1 < r/r_{drop} < 10$. Figure 15b provides the concentration for the intermediate species generated during MD combustion. As shown, the peak concentration has the following relationship: $Y_{C2H4} > Y_{C2H2} > Y_{C3H6} > Y_{1-C4H8} > Y_{CH4}$. The subset to Fig. 15b shows the concentrations for major radicals evolved from MD in the burning process. At this stage ($t = 0.0053$ s), the concentration for these radicals are as high as the order of 10–100 ppm.

Figure 16a shows the spatio-temporal distribution at $t = 0.10$ s. As shown, the maximum temperature, now around 2100 K, is lower than it was at $t = 0.0053$ s due to transient heat dissipation. The maximum temperature occurs at a larger r/r_{drop} than at 0.0053 s meaning the FSR has increased at this stage. The boundary layer thickness of MD and oxygen and all the other species expand to around $r/r_{drop} = 40$. Major products all have higher concentrations as shown in Fig. 16b, but the inset shows that the concentrations for MD-based radicals have gone down to less than 10 ppm. The CH_4 concentration becomes higher than that of $1-C_4H_8$ at $t = 0.10$ s. Figures 17 and 18 show the spatio-temporal distribution for $t = 0.30$ s and $t = 0.50$ s, respectively. As shown, the diffusion and thermal boundary layer keep expanding with time. At $t = 0.50$ s, the peak concentration of C_2H_2 starts to decrease and the concentration for $1-C_4H_8$ become slightly higher than that of CH_4.

Figure 19 shows the path flux analysis of MD at the flame location to summarize MD's combustion reactions during burning. The path flux analysis shows that the bulk of the fuel goes through H abstraction reactions, which amounts up to about 73% of the fuel consumption. The main abstracting radical is found to be H atom, followed by OH radical. The large amount of abstraction reaction is typical of high temperature oxidation systems, and is similar to that observed in CFF as well. MD2J signifies the most major compound that is directly generated from MD combustion (10% of MD

is converted into MD2J). The second major path is MD to MDMJ (8%) and the reactions that produce MD3J, MD4J,...,MD9J occupy same amount of the flux path (7%).

5. Conclusions

Fiber-supported droplet combustion experiments are carried out in an environment that promotes spherical symmetry for MD droplet flames with initial droplet diameters of ~0.55 mm. The experimental results agree with the predictions provided by detailed numerical simulations within the error bars.

The droplet flame of MD has a clear blue boundary with visible yellow inner core also observed. There is no visible soot shell formation or particulate aggregates visible for this size of MD droplet with the lighting setup of this study. Results of droplet size evolution show that MD droplet combustion burning rate reaches a quasi-steady value of 0.6 mm²/s.

Detailed numerical simulation was used to investigate the effect of fiber size, thermal conductivity and Nusselt number for the tether fiber on the burning rate of a MD droplet. Results show that these parameters have very minimal effect on the droplet combustion history. Predicted species and temperature distributions along the radial direction provide more understanding for this transient problem coupled with phase equilibrium, fuel vaporization, and chemical reactions. The comparison between experimental and numerical droplet combustion variables for the spherically symmetric case shown in this study also provided validation for the MD models that involved chemical kinetics proposed previously [28] and heat and mass transfer associated with multi-phase combustion, which is a corner stone to developing detailed models for multiphase combustion of ester-based bio-fuels. Additional work is needed to expand the database of single droplet combustion under carefully controlled and modelable conditions.

Acknowledgments

References

[1] Transforming Combustion Research Through Cyberinfrastructure, Committee on Building Cyberinfrastructure for Combustion Research, National Research Council, The National Academies Press, April 2011. ISBN-13: 978-0-309-16387-3. <http://www.nap.edu/catalog.php?record_id=13049>.
[2] A Workshop to Identify Research Needs and Impacts in Predictive Simulation for Internal Combustion Engines (PreSICE), Office of Energy Efficiency and Renewable Energy, Office of Science, U.S. Department of Energy. <http://www1.eere.energy.gov/vehiclesandfuels/pdfs/presice_rpt.pdf> (03.03.11).
[3] K. Chakravarthy, J. McFarlane, S. Daw, Y. Ra, R. Reitz, J. Griffin, SAE Paper no. 2007-01-4030.
[4] P. Dagaut, S. Gaïl, J. Phys. Chem. A 111 (2007) 3992–4000.
[5] K.L. Pan, J.W. Li, C.P. Chen, C.H. Wang, Combust. Flame 156 (2009) 1926–1936.
[6] J. Patterson, M.G. Hassan, A. Clarke, G. Shama, K. Hellgardt, R. Chen, SAE Paper no. 2006-01-0234.
[7] J. Krahl, A. Munack, D. Bockey, Landbau. Völken. 57 (2007) 415–418.
[8] M. Pagliaro, M. Rossi, The Future of Glycerol, RSC Publishing, Cambridge, p. 11.
[9] A.K. Agarwal, Prog. Energy Combust. Sci. 33 (2007) 233–271.
[10] O. Herbinet, W.J. Pitz, C.K. Westbrook, Combust. Flame 154 (2008) 507–528.
[11] O. Herbinet, W.J. Pitz, C.K. Westbrook, Combust. Flame 157 (2010) 893–908.
[12] P. Dagaut, S. Gaïl, M. Sahasrabudhe, Proc. Combust. Inst. 31 (2007) 2955–2961.
[13] Y. Ra, R.D. Reitz, J. McFarlane, C.S. Daw, SAE Paper no. 2008–01-1379.
[14] S. Dooley, S.H. Won, M. Chaos, J. Heyne, Y. Ju, F.L. Dryer, K. Kumar, C.J. Sung, H. Wang, M.A. Oehlschlaeger, R.J. Santoro, T.A. Litzinger, Combust. Flame 157 (2010) 2333–2339.
[15] K. Anand, Y. Ra, R.D. Reitz, B. Bunting, Energy Fuels 25 (2011) 1474–1484.
[16] E.M. Fisher, W.J. Pitz, H.J. Curran, C.K. Westbrook, Proc. Combust. Inst. 28 (2000) 1579–1586.
[17] S. Gaïl, M.J. Thomson, S.M. Sarathy, S.A. Syed, P. Dagaut, P. Diévart, A.J. Marchese, F.L. Dryer, Proc. Combust. Inst. 31 (2007) 305–311.
[18] K. Seshadri, T. Lu, O. Herbinet, S. Humer, U. Niemann, W.J. Pitz, R. Seiser, C.K. Law, Proc. Combust. Inst. 32 (2009) 1067–1074.
[19] A.A. Amsden KIVA-3V, Release 2, Improvements to KIVA-3V, 1999, LA-UR-99-915.
[20] R.J. Kee, F.M. Rupley, J.A. Miller, Sandia Report No. SAND 89–8009, 1989.
[21] J.P. Szybist, A.L. Boehman, D.C. Haworth, H. Koga Combust, Flame 149 (2007) 112–128.
[22] J.P. Szybist, J. Song, M. Alam, A.L. Boehman, Fuel Process. Technol. 88 (2007) 679–691.
[23] W.A. Sirignano, Fluid Dynamics and Transport of Droplets and Sprays, Cambridge University Press, 1999. pp. 10–21.
[24] C.T. Avedisian, Soot formation in spherically symmetric droplet combustion, in: R. Sawyer, F.L. Dryer (Eds.), Physical and Chemical Aspects of Combustion, Gordon and Breach Publ., 1997. pp. 135–160 (Chapter 6).
[25] Y.C. Liu, C.T. Avedisian, Combust. Flame 159 (2012) 770–783.
[26] T. Farouk, F.L. Dryer, Combust. Flame 159 (2012) 3208–3223.
[27] A.J. Marchese, T.L. Vaughn, K. Kroenlein, F.L. Dryer, Proc. Combust. Inst. 33 (2011) 2021–2030.
[28] P. Diévart, S.H. Won, S. Dooley, F.L. Dryer, Y. Ju, Combust. Flame 159 (2012) 1793–1805.
[29] J.H. Bae, C.T. Avedisian, Combust. Flame 145 (2006) 607–620.
[30] C.T. Avedisian, B.J. Callahan, Proc. Combust. Inst. 28 (2007) 991–997.
[31] C.L. Dembia, Y.C. Liu, C.T. Avedisian, Image Anal. Stereol. 31 (2012) 137–148.
[32] A. Cuoci, M. Mehl, G. Buzzi-Ferraris, T. Faravelli, D. Manca, E. Ranzi, Combust. Flame 143 (2005) 211–226.
[33] K. Kroenlein, Ph.D. Thesis, Depart. of Mech. and Aero. Engr., Princeton University, 2007.
[34] T. Farouk, F.L. Dryer, Combust. Flame 159 (2012) 200–209.
[35] C.K. Westbrook, W.J. Pitz, H.J. Curran, J. Phys. Chem. A 110 (2006) 6912–6922.
[36] F.P. Incropera, D.P. DeWitt, Introduction to Heat Transfer, 4th ed., 2002, p. 824.
[37] G.E. Youngblood, D.J. Senor, W. Kowbel, J. Webb, A. Kohyama, Thermophysical and Mechanical Properties of SiC/SiC Composites, Semiannual Progress report for Period Ending, US DOE, Office of Fusion Energy Sciences, Washington, DC, DOE/ER-0313/27, December 31, 1999, pp. 113–118.
[38] A.J. Whittaker, M.L. Allitt, D.G. Onn, J.D. Bolt, in: C.J. Cremers, H.A. Fine (Eds.), Thermal Conductivity vol. 21, 1990, pp. 187–198.